Check for updates

View Article Online
View Journal

Nanoscale

Accepted Manuscript

This article can be cited before page numbers have been issued, to do this please use: M. Erzina, D. E. Votkina, E. Miliutina, O. Gorin, M. Y. S. Ibrahim, T. Friedl, D. Köpfler, C. Koller, M. M. Muhammed, J. H. Mokkath, M. Valtiner, O. Lyutakov and O. Guselnikova, *Nanoscale*, 2025, DOI: 10.1039/D5NR03832D.

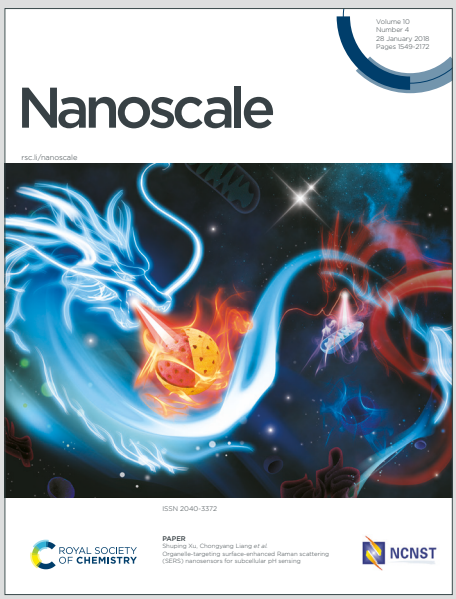

This is an Accepted Manuscript, which has been through the Royal Society of Chemistry peer review process and has been accepted for publication.

Accepted Manuscripts are published online shortly after acceptance, before technical editing, formatting and proof reading. Using this free service, authors can make their results available to the community, in citable form, before we publish the edited article. We will replace this Accepted Manuscript with the edited and formatted Advance Article as soon as it is available.

You can find more information about Accepted Manuscripts in the Information for Authors.

Please note that technical editing may introduce minor changes to the text and/or graphics, which may alter content. The journal's standard Terms & Conditions and the Ethical guidelines still apply. In no event shall the Royal Society of Chemistry be held responsible for any errors or omissions in this Accepted Manuscript or any consequences arising from the use of any information it contains.

ROYAL SOCIETY OF CHEMISTRY

rsc.li/nanoscale

View Article Online
DOI: 10.1039/D5NR03832D

From Batch to Flow Plasmon Catalysis: Revealing Mass Transport Limits in Au@Pd Nanocatalysts for Suzuki Coupling

Mariia Erzina[a†], Daria Votkina[b†], Elena Miliutina[a], Oleg Gorin[a], Malek Y. S. Ibrahim[c], David M. Köpfler[c], Tobias Friedl[d], Christian Koller[d,e], Junais Habeeb Mokkath[f], Mufasila Mumthaz Muhammed[g], Markus Valtiner[h], Oleksiy Lyutakov[a], Olga Guselnikova[b,h*]

[a] Department of Solid-State Engineering, University of Chemistry and Technology, Technicka 5, Prague 166 28, Czech Republic

[b] Research School of Chemistry and Applied Biomedical Sciences, Tomsk Polytechnic University, Lenina Avn. 30, Tomsk, 634050, Russian Federation

[c] Redeem Solar Technologies GmbH, Sandgasse 36/IV, 8010 Graz, Austria

[d] University of Applied Sciences Wiener Neustadt, Johannes Gutenberg-Straße 3, 2700 Wiener Neustadt, Austria

[e] Fotec - Forschungs- und Technologietransfer GmbH, Wiener Neustadt, Viktor Kaplan-Straße 22700 Wiener Neustadt Austria

[f] College of Integrative Studies, Abdullah Al Salem University, Khaldiya campus, Kuwait

[g] College of Engineering, International University of Science and Technology in Kuwait, Ardiya, Kuwait

[h] Vienna University of Technology, Institute of Applied Physics, Karlsplatz 13, 1040 Vienna, Austria

Open Access Article. Published on 12 December 2025. Downloaded on 1/21/2026 11:08:48 PM.
This article is licensed under a Creative Commons Attribution 3.0 Unported Licence.

Nanoscale Accepted Manuscript

Abstract

Plasmonic catalysis, as a powerful tool for synthetic transformations, has the potential to impact wide-scale applications by converting solar light into energy for chemical reactions. Current studies are limited to mL-scale batch reactors with mg-level nanocatalysts, lacking feasibility at common laboratory and industrially configurations. To overcome this limitation, transition of plasmonic chemistry from batch to flow mode is foreseen, however, there is a lack of understanding of how plasmon-driven processes couple with mass transport. To address this, we designed plasmonic catalysts for a flow system within tens of mL scale employing gram-scale Au@PdNPs-Al_2O_3 nanostructures in a flow reactor. Using Suzuki cross-coupling as a model reaction, we showed that flow mode for Au@PdNPs-Al_2O_3 increases reaction rate, time to full conversion and apparent quantum yield (AQY) ×3 times compared to batch mode and overperform previously reported ones. Fluid dynamic simulations showed critical effect of residence times of nanocatalyst–reactant complexes under illumination to product yield. This was consistent with photocurrent measurements, revealing electron transfer efficiency is enhanced under increased mass transport conditions. Unlike prior studies that primarily emphasized the carrier dynamic within metal–metal/semiconductor heterojunctions (e.g., Au/Pd) in batch mode, our flow system demonstrates that efficient carrier transfer to reactants is critical for achieving high TON and AQY. This work provides the first framework for translating plasmonic catalysis into flow, offering design principles for future light-driven chemical processes beyond conventional batch mode.

Keywords: plasmon, plasmon catalysis, Suzuki coupling, flow reactor, mass transport

Corresponding author: olga.guselnikova@tuwien.ac.at

View Article Online
DOI: 10.1039/D5NR03832D

Open Access Article. Published on 12 December 2025. Downloaded on 1/21/2026 11:08:48 PM.
This article is licensed under a Creative Commons Attribution 3.0 Unported Licence.

Introduction.

Plasmon catalysis using low-energy consuming nanostructure is a powerful tool for synthetic transformations[1,2], which has the potential to impact industrial applications[3,4]. It enables the energy transfer from nanoparticles to molecules through non-thermal mechanisms like hot carrier moving and intramolecular electron excitation, as well as through thermal effects like plasmonic heating[5,6]. The main appeal of plasmon-assisted chemistry lies in developing low-cost, sustainable technologies that harness solar energy to produce high-value chemicals[7,8]. Recent advances focus on designing plasmonic catalysts[9] that enhance photocatalytic efficiency through synergy between active sites and plasmonic excitation[2,10]. For instance, plasmon-enhanced photochemical ethylene oxide production has been explored as an industrially relevant process[11], while plasmon-driven azide-alkyne cycloaddition has been demonstrated as a sustainable approach to copper-free click chemistry[12,13]. At the same time, Suzuki cross-coupling reactions have been developed as a key strategy for carbon-carbon bond formation in industrial and pharmaceutical applications[14,15]. Suzuki reaction has been also probed under plasmonic catalytic conditions[16-22].

One of the major bottlenecks in plasmonic catalysis is the lack of scalability demonstrations, as most studies remain limited to small-scale trials without addressing scale-up[1,3,8]. Most of recent reports on plasmon catalysis for organic transformations utilize a few mL reaction volume in a various configuration batch mode reactor using mg-scale dispersed plasmonic nanocatalysts. Currently, there is a lack[23,24] of quantitative feasibility studies on plasmonic catalytic processes at relevant industrial or at least closed to industrial configuration. However, the challenge here is beyond technological scale-up, but in a fundamental issue - the inefficient mass transport at the solid (nanocatalyst)-liquid interface in a batch mode. The plasmon-enhanced reactions often rely on localized hotspots, leading to severe diffusion limitations. These mass transport constraints arise due to the inefficient diffusion of reactants to plasmonic hotspots, particularly in high photon flux environments, where reactants are depleted faster than they are replenished from the bulk solution. This phenomenon creates a diffusion-controlled regime recently suggested by Alberto Naldoni[25], ultimately leading to limited reaction rates despite the availability of hot carriers.

In order to solve this limitation, the challenge could be broken down to probing the relevant reactor configuration and relevant plasmonic nanocatalysts synthesis. The industrial configuration for plasmon catalysis could be borrowed from classic photocatalysis setup[26,27], where there are some showcases, such as synthesis of Vitamin D, caprolactam, and rose oxide, the latter estimated at tons level annually[28]. For example, Can Li developed a direct solar array-type flat-plate photochemical reaction system with a reaction area of 5 m^2 with PerfectLight company[29]. Thus, one could attempt to apply the lessons learned on mechanistic studies[27,30] to upscaled plasmonic nanosystems.

As an alternative solution for plasmon catalysis, plasmon-driven chemistry is tested in continuous-flow reactors with Au@Pd-based plasmonic catalyst. We probed plasmon-driven Suzuki-cross coupling as representative example of one of the scenarios for plasmonic chemistry. For flow reactor experiments, we prepared in g-scale plasmonic nanoparticles based on commercial Al_2O_3 via microwave assisted AuNPs growth and thin Pd layer reduction. These Au@PdNPs-Al_2O_3 were used in tens of mL volume for plasmonic Suzuki coupling. We hypothesize that mass transfer processes governing carrier delivery to reactants are critical for efficient photon utilization, a factor largely overlooked in previous plasmonic studies. By integrating lessons from plasmonic reaction kinetics, photon penetration, and mass transport limitations, upscaled plasmonic experiments were tailored to maximize the benefits of plasmonic energy conversion in flow.

Nanoscale Accepted Manuscript

View Article Online
DOI: 10.1039/D5NR03832D

Results and discussion

1. Gram-scale synthesis of plasmonic catalysts

We commenced our investigation with the synthesis of plasmonic catalysts based on commercially available Al_2O_3 porous materials (0.58 nm pore size, 22±1.5 μm particle size) served as a support for plasmon active AuNPs deposition (Fig. 1A,B). High surface area materials provide a platform for the plasmonic NPs deposition[31].

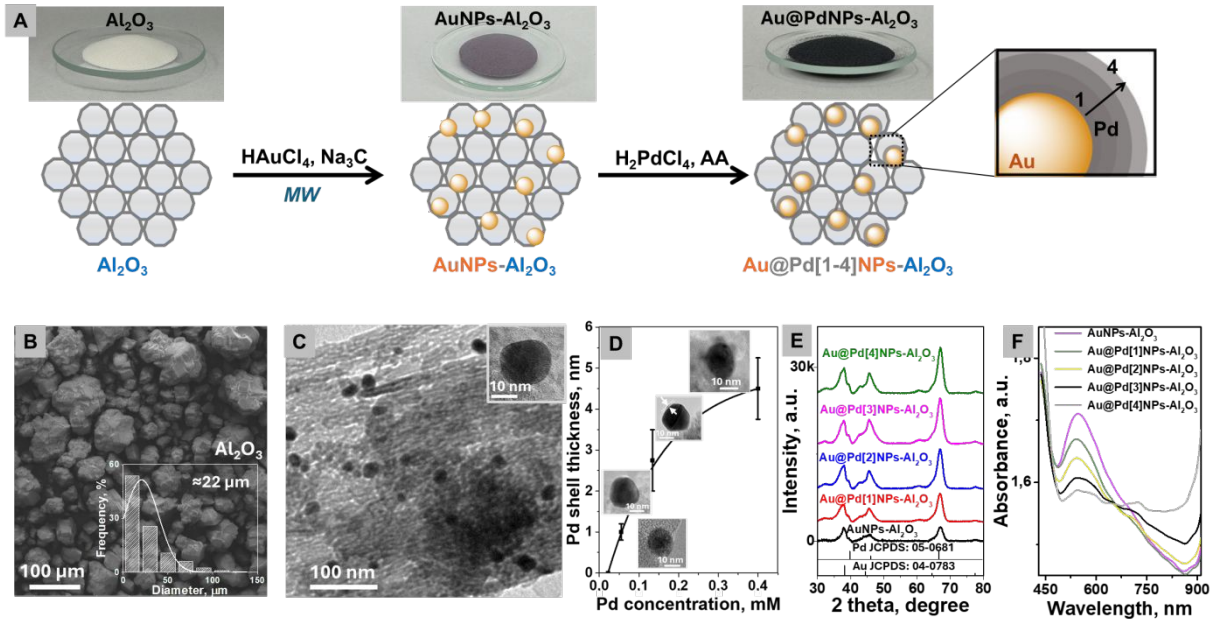

Figure 1. A – fabrication of Au@PdNPs-Al_2O_3 on a gram-scale, B – SEM image of pristine Al_2O_3 (insert - size distribution), C – TEM image of AuNPs-Al_2O_3, D - Pd shell thickness against Pd concentration (error bars indicate standard deviation from ≈ 100 particles per sample), E - XRD pattern of prepared AuNPs-Al_2O_3 and Au@Pd[1-4]NPs-Al_2O_3, F – UV-Vis spectra of prepared AuNPs-Al_2O_3 and Au@Pd[1-4]NPs-Al_2O_3

AuNPs were deposited on Al_2O_3 by microwave assisted approach[32] using sodium citrate as reducing agent (Fig. S1). In contrast to common complex multi-step synthesis routes[9], this microwave-assisted straightforward technique is highly promising for across laboratories testing, thus shortening the timeline for them to have a broad impact[7]. The gold nanoparticles sized by 20±3 nm deposited on the Al_2O_3 surface exhibited a spherical morphology (Fig.1C). The next step of Pd deposition was also realized in a gram-scale *via* the reduction of H_2PdCl_4 with ascorbic acid[33,34].

We prepared a set of Au@Pd[1-4]NPs-Al_2O_3 *via* addition of different amount of Pd precursor and characterized by transmission electron microscopy (TEM) (Fig.1D, Fig.S2), X-ray diffraction (XRD) (Fig.1E), ultraviolet–visible spectroscopy (UV-Vis) (Fig.1F) and atomic absorption spectrophotometry (AAS) (Table S1). TEM image of prepared AuNPs-Al_2O_3 shows the formation of spherical nanoparticles (Fig. 1C). After Pd precipitation on the surface of AuNPs -Al_2O_3, the dependence of Pd shell thickness on Pd concentration (H_2PdCl_4) of Au@Pd[1-4]NPs-Al_2O_3 were analysed (evaluated from a gradual increase of Au@Pd size, estimated from TEM measurements). The dependence has a nonlinear increase in shell thickness with increasing Pd concentration, indicating a saturation-like growth (Fig. 1D, Fig. S2). With increase of Pd, the average diameter of Au@PdNPs deposited on Al_2O_3 nanoparticles increases from 20±2 nm for Au@Pd[1]NPs-Al_2O_3 to 30±3 nm for Au@Pd[4]NPs-Al_2O_3 indicating the growth of Pd shell on the surface of AuNPs-Al_2O_3, confirmed by AAS (Fig.

Open Access Article. Published on 12 December 2025. Downloaded on 1/21/2026 11:08:48 PM.
This article is licensed under a Creative Commons Attribution 3.0 Unported Licence.

Nanoscale Accepted Manuscript

View Article Online
DOI: 10.1039/D5NR03832D

1D, Table S1). The X-ray diffraction (XRD) pattern of prepared Au@Pd-Al_2O_3 sample is shown in Figure 1E. It is evident that the sample contain face-centered cubic Pd because the peaks at 40.5°, 46.8°, 68.4°, corresponding to the (111), (200), (220) lattice planes, are observed (the JCPDS card №. 05-0681) (Fig. 1E). So, it is clear that most of the strong diffraction peaks of Pd almost overlap with the peaks of Au at 38.2°, 44.9° and 64.6°, which correspond to (111), (200) and (220) (the JCPDS card №. 05-04783)[35,36].

The set of prepared materials Au@Pd[1-4]NPs-Al_2O_3 was characterized by UV-Vis absorption spectroscopy (Fig. 1F). The absorbance of the catalyst and pristine AuNPs-$Al_2O_3$was recorded in water/ethanol solution to probe the plasmonic response under the same liquid-phase conditions used for catalysis. This approach enables us to capture solvent- and interface-dependent spectral shifts[37].The last has well-recognized absorbance peak at 550 nm that corresponds to plasmon resonance of spherical gold nanoparticles with 20 nm diameter loaded onto Al_2O_3. Deposition of Pd layer in the catalyst system led to AuNPs absorbance drop and rise of a new absorbance maximum at the ≈ 700 nm region that could be attributed to the hybridization in Au–Pd interface that covers Au[38].

2. Probing Pd shell thickness towards maximum catalytic performance (batch mode) via experimental and theoretical approaches

Based on UV-Vis spectra we chose LED with the excitation wavelength of 690 nm for the further catalytic experiments (Fig. S3). Longer wavelengths (>600 nm) could penetrate more deeply into the reaction media, providing a more uniform activation of photocatalysts and substrates. This is especially beneficial for large-scale industrial applications[3]. The prepared Au@Pd[1-4]NPs-Al_2O_3 were tested in Suzuki coupling reaction between bromobenzene and phenylboronic acid under light irradiation at 690 nm (300 mW/cm²) in a batch mode with 20 mL reaction volume (Fig. 2A, B). Analytical yield of biphenyl was verified by gas chromatography (GC) after 4 hours of reaction with preliminary calibration for quantitative analysis (Fig. S4,5). Based on Fig. 2B, AuNPs-Al_2O_3 show minimal catalytic activity, while introduction of Pd doubles the product yield (Fig. 2B). However, the increase of Pd shell beyond 3 nm (Au@Pd[3]NPs-Al_2O_3) does not lead to further catalytic performance improvement.

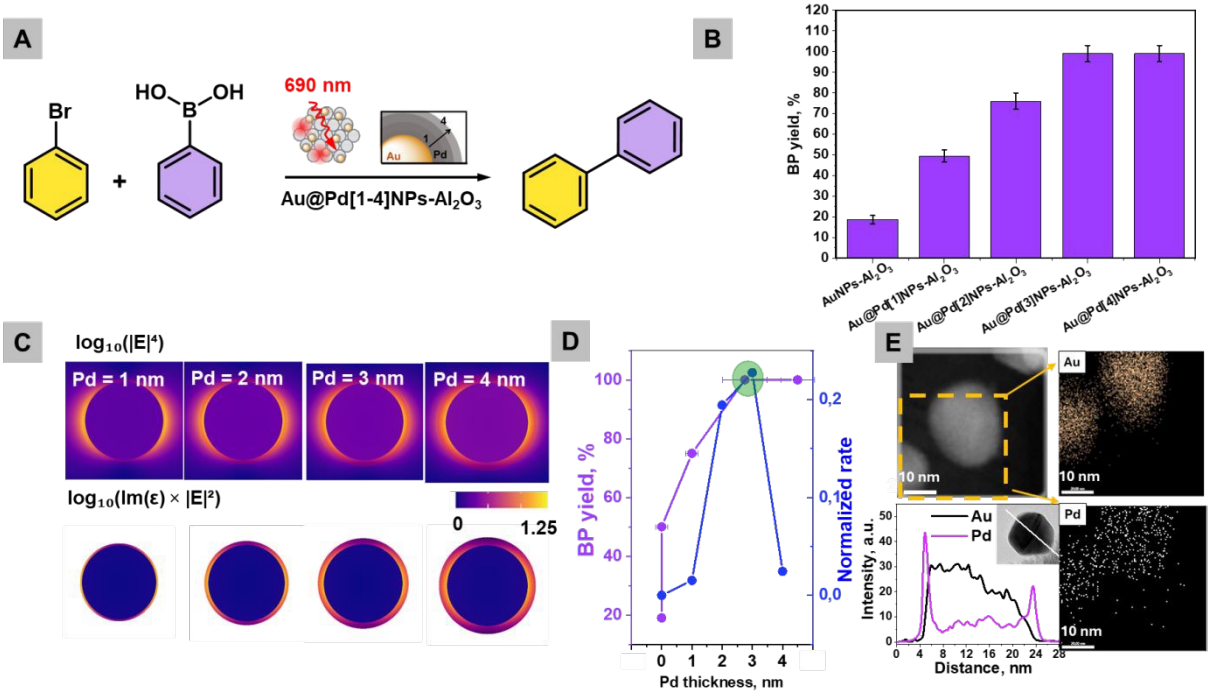

Open Access Article. Published on 12 December 2025. Downloaded on 1/21/2026 11:08:48 PM.
This article is licensed under a Creative Commons Attribution 3.0 Unported Licence.

Nanoscale Accepted Manuscript

View Article Online
DOI: 10.1039/D5NR03832D

Figure 2. A – scheme of Suzuki cross coupling using Au@Pd[1-4]NPs-Al_2O_3 , B – BP analytical yield (GC measured) in 4 hours of reaction using Au@Pd[1-4]NPs-Al_2O_3 (yield are means and error bars represent the standard deviation from three independent measurements (n = 3)), C - Simulated near-field electromagnetic enhancement (top row) and hot carrier generation maps (bottom row) for single Au@Pd nanoparticles with a 20 nm Au core and varying Pd shell thicknesses (1–4 nm), D - Correlation between Pd shell thickness (20 nm Au core), experimental catalytic performance (BP yield after 4 hour reaction), and simulated Suzuki coupling activity, E - STEM-EDX mapping images of an individual nanoparticle of Au@PdNPs-Al_2O_3 and its elemental line profile

To explain the experimentally determined optimal Pd thickness of Au@Pd[3]NPs-Al_2O_3, simulations of electromagnetic field (EM) enhancement and hot electron generation rates were performed (Fig. 2C). Firstly, the absorption cross-section of Au@Pd with increasing Pd shell thicknesses was calculated by T-matrix method (Fig. S6)[39], which solves Maxwell's equations for spherical multilayered particles by decomposing the fields into vector spherical harmonics. The slight dissiperancy between Fig. S6 and 1F is explained by neglecting Al_2O_3 support and solvent interface effects. However, the red shift is observed with Pd shell growing similar to experiental UV-Vis spectra on Figure 1F. Upon coating with Pd, the absorption spectra exhibit a progressive redshift with increase of thickness from 1 to 4 nm that occurs due to Pd shell' significant plasmon damping and dielectric screening[40]. Figure 2C (upper row) presents the simulated Raman enhancement factor (EF), approximated as $\log_{10}(|E|^4)$. The enhancement maps reveal that near-field hotspots are initially localized at the outer shell, but both their intensity and spatial extent diminish as the Pd shell thickens increase due to increased absorption and suppression of LSPR by Pd[40].

The simulated hot carrier distribution, expressed as $\log_{10}(\mathrm{Im}(\varepsilon) \times |E|^2)$ that serves as a qualitative indicator of the local generation rate of hot electrons and holes driven by plasmon-induced intraband and interband transitions[41] (Fig. 2C, lower row), with Im(ε) representing the imaginary part of the local dielectric function and $|E|^2$ reflecting the local field intensity enhancement. Simulated hot carrier distributions reveal that carrier generation becomes increasingly concentrated at the Au–Pd interface and Pd surface with thicker shells, owing to Pd's high Im(ε)[42,43]. This indicates Pd acts as a plasmonic energy sink, enabling localized carrier excitation. With all these results in hand, the rate profile for Au@Pd-Al_2O_3 nanoparticles were simulated and exhibited a clear maximum in catalytic activity at a Pd shell thickness of ~ 3 nm for a fixed 20 nm Au core (Fig. 2D). Simulated Suzuki activity (Fig. 2D) refers to a calculated relative rate constant derived from an Arrhenius-type kinetic model where the activation barrier is modulated by both hot-carrier flux decay through the Pd shell and plasmonic absorption enhancement. The observed trends are consistent with prior studies such as those by Christopher et al.[42] and Baffou et al.[43], who demonstrated that plasmonic-catalytic hybrid structures generate hot carriers primarily in regions with high loss (Im(ε)) and field overlap. This trend arises from a balance between hot-carrier flux, and plasmonic absorption, and suggests an optimal geometry where the shell is thick enough to provide a catalytically active amount of Pd but thin enough to permit efficient hot-carrier transfer from the Au core.

Therefore, experimental and theoretical studies showed that Au@Pd[3]NPs-Al_2O_3 (abbreviated as Au@PdNPs-Al_2O_3 further) with ≈3 nm Pd thickness are optimal for the further catalytic studies (Fig. 2D). Notably, due to the efficient light-induced charge separation and surface activation facilitated by the plasmonic core–shell configuration, only trace amounts of Pd (0.09 wt % according to AAS) were sufficient for successful Suzuki coupling. The time-resolved GC measurements of Suzuki coupling in batch mode show that after 11 h, the high yield of biphenyl

Open Access Article. Published on 12 December 2025. Downloaded on 1/21/2026 11:08:48 PM.
This article is licensed under a Creative Commons Attribution 3.0 Unported Licence.

Nanoscale Accepted Manuscript

View Article Online
DOI: 10.1039/D5NR03832D

is obtained (Fig. 2B). The best-performing Au@PdNPs-Al_2O_3 were additionally characterized by STEM-EDX analysis (Fig. 2E) of an individual nanoparticle of Au@PdNPs clearly indicates the homogeneous distribution of both Au and Pd. The formation of the core–shell structure is further supported by the elemental line profile (Fig. 2E) obtained from a selected single particle in STEM mode. The experimentally measured 2.7±0.7 nm thickness of Au@PdNPs-Al_2O_3 (estimated as the width of two concentration peaks, located at the nanoparticle edges and corresponded to Pd shell) slightly deviate from theoretically predicted optimal of 3 nm. However, the overall trend on Figure 2D between experimentally measured and simulated correspond each other. Additionally, X-ray photoelectron spectroscopy (XPS) analysis showed that Au@PdNPs- Al_2O_3 has only 0.6 at. % Pd surface concentration (Fig. S7). The Au 4f spectrum in Figure S7B shows deconvoluted doublet with peaks at 87.8 eV and 84.3 eV that can be assigned to $4f_{5/2}$ and $4f_{7/2}$, respectively[44]. The successful loading of palladium is evidenced by the Pd 3d spectrum (Fig. S7C): two fitted peaks positioned at 340.5 eV and 335.5 eV correspond to the Pd $3d_{3/2}$ and $3d_{5/2}$ spin–orbit levels of palladium (0)[45], confirming that Pd is deposited in non-oxidized form. This approach aligns with current demands for reducing the reliance on scarce and expensive metals, while leveraging nanoscale engineering to maintain catalytic efficiency. Such design is especially valuable in photocatalytic systems where plasmonic activation can compensate for the lower catalyst loading by enhancing local electric fields and surface reaction rates.

3. Suzuki C-C coupling flow mode experimental setup and optimization

A flat-plate, continuous-flow photoreactor (Arrow Reactor model) from Redeem Solar Technologies GmbH was employed in this study. The reactor is constructed from stainless steel and contains a rectangular flow channel (Fig. 3A). This channel design was chosen over a linear flow-through configuration to improve light utilization and reaction efficiency. In a straight channel, laminar flow causes uneven photon penetration and limited mixing of catalyst particles. The arrow-shaped inserts disrupt this flow, generating recirculation zones and vortices that (i) extend catalyst residence time in the illuminated zone[46], (ii) homogenize light exposure, and (iii) enhance convective transport of reactants[47]. We intentionally used low-power LED (<1000 mW/cm²) to ensure that thermal effects (plasmonic heating) are minimized[48]. Therefore, we expect that the system remains in a “purely photonic” regime, where any catalytic enhancement is due to hot charge carriers, not heat, to exclude the heat-driven Suzuki coupling. Additionally, the usage of cooler fan allowed to keep constant temperature at <30 °C during plasmon-assisted reaction. The thermocamera image shows insignificant heating of reactor to a maximum temperature 27.8 °C during irradiation (Fig. S8).

3.1. Experimental flow reactor setup

The experimental set-up is presented in Figure 3A (photo is given in Fig. S8) and contains 1 - photoreactor wall –containing inside Au@PdNPs-Al_2O_3 nanoparticles suspension; 2 - light source 690 nm LED, beam with a 10 mm diameter directed at the catalytic surface, 3 - peristaltic pump – circulates the reaction mixture through the illuminated zone, 4 - reaction flask, that contains the substrate mixture and serves as a reservoir for the liquid-phase reactants and products, 5 - magnetic stirrer and 6 - ventilator. Initially, the reaction mixture (catalyst, reagents and solvents) was loaded into stock flask equipped with magnetic bar to minimize the precipitation of catalyst.

Open Access Article. Published on 12 December 2025. Downloaded on 1/21/2026 11:08:48 PM.
This article is licensed under a Creative Commons Attribution 3.0 Unported Licence.

Nanoscale Accepted Manuscript

View Article Online
DOI: 10.1039/D5NR03832D

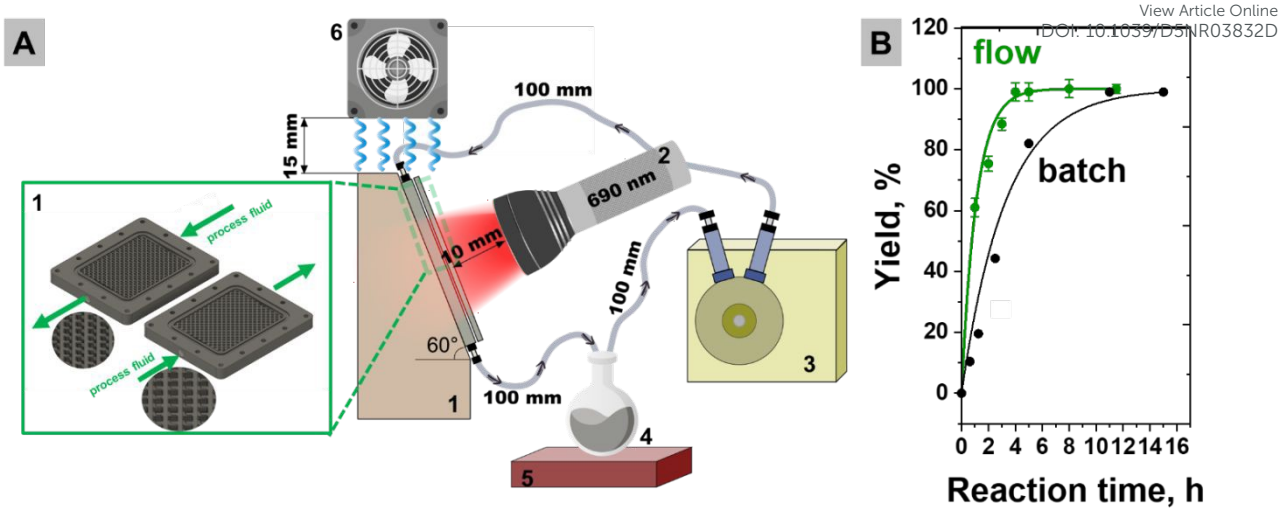

Figure 3. A - Schematic illustration of the plasmonic flow reactor setup used for visible-light-driven Suzuki coupling reactions: 1 - flow reactor, 2 - 690 nm LED, 3 - peristaltic pump, 4 - stock flask, 5 - magnetic stirrer, 6 - ventilator. B - kinetic curves of biphenyl formation using Au@PdNPs-Al_2O_3 in batch mode and flow reactor (optimized parameters of 60 mL/min, green arrows point upstream and backward flow) using 300 mW/cm² irradiance (yields are means and error bars represent the standard deviation from three independent measurements (n = 3)).

Within the photochemical flow reactor, we repeated the same time-resolved measurements of Suzuki coupling of 20 mL total reaction volume (Fig. 3B). Samples were taken in regular time intervals from the collection vessel and the GC measured analytical yield was plotted for all the reactors against time of circulation. During circulation, the flow reactor was illuminated with the same LED (690 nm) and light irradiance was kept at a constant level (300 mW cm^{-2}). The initial concentration of substrate, catalyst, and water was also kept constant for all the flow and batch experiments. Figure 3B shows the comparison of time-resolved biphenyl formation profiles for both the flow reactor and batch (flask) experiments. The flow system demonstrates a significantly steeper initial rate (2.7×10^{-4} for flow and 1.05×10^{-4} s^{-1} for batch reactors, Fig. S9) with quantitative yield after 4 hours, highlighting the catalytic advantages of improved mass and photon transfer under flow conditions (Fig. S5, Suppl.Note1). Therefore, further control experiments were also conducted for 4 hours. The control experiment in the dark and with illumination at 690 nm in the absence of NPs showed lower conversion and yield of 45 % and <1%, correspondently.

3.2. Experimental and computational fluid dynamics (CFD) analysis towards plasmonic reaction optimization

To optimize plasmon-enhanced catalysis, we combined experiments and CFD analysis on the tilted photoflow reactor (Figures 4). Flow direction (forward vs. backward) and arrows point (downstream vs. upstream), residence time, and convective mass transfer were systematically studied, as potential parameters, which can directly affect hot carrier utilization at the metal–reactant interface. The basic model parameters are shown Fig. S10 and Suppl. Note 2. While a full spatially resolved model coupling catalyst distribution, reactant concentration gradients, and photon absorption would provide deeper mechanistic insight, such an approach would be beyond the scope of this work. We envision establishing such a “catalyst–reactant–photon” distribution model represents an important direction for future studies.

Open Access Article. Published on 12 December 2025. Downloaded on 1/21/2026 11:08:48 PM.
This article is licensed under a Creative Commons Attribution 3.0 Unported Licence.

Nanoscale Accepted Manuscript

View Article Online
DOI: 10.1039/D5NR03832D

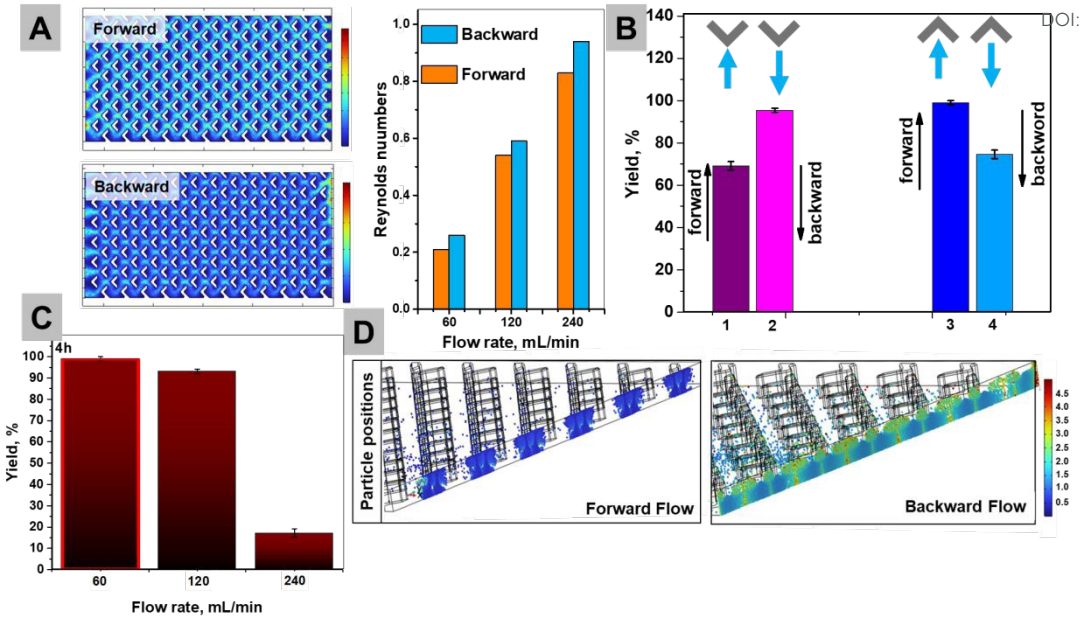

Figure 4. A – CFD simulations of Reynolds number of areas in cross-section for 60 ml/min of forward (top) and backward (bottom) flow rate. The column bars represent the summarized Reynolds numbers from different models. B - Effect of flow (60 mL/min) direction and arrow orientation on plasmon-driven Suzuki coupling (biphenyl yields after 4 h of 690 nm illumination): 1) arrows point downstream and backward flow; 2) arrows point downstream and forward flow; 3) arrows point upstream and backward flow; 4) arrows point upstream and and forward flow (yields are means and error bars represent the standard deviation from three independent measurements ($n = 3$)), C – Simulated positions of catalyst particles after 5 s at 60 mL/min flow rate. Color indicates residence time, with brighter areas corresponding to longer exposure in the illuminated zone.

CFD simulations (Fig. S10-12) and experiments revealed that flow orientation (Fig. 4A,B) strongly influenced hydrodynamics and catalytic performance. At identical flow rates (300 rpm), the backward configuration showed a higher average Reynolds number (Table S2) than the forward mode, indicating enhanced bulk mixing despite a slightly lower Re_{max} (9.89 vs. 12.9). Although both regimes remained laminar (Re < 2300), the improved convective flow in backward mode reduced mass transport limitations, leading to ~90 % product yield versus ~70 % in forward flow (Table S2). Tracer simulations confirmed that gravitational effects were negligible, with the improvement arising purely from favorable convective patterns[49].

To experimentally evaluate the role of flow rate on catalytic efficiency, reactions were conducted at three different rates: 60, 120, and 240 ml/min (Fig. 4C). The highest yield of 99% was achieved at 60 ml/min, which corresponds to a slower flow rate and longer residence time. At 120 ml/min, a moderate decrease in yield to 93% was observed, while at 240 ml/min the reaction performance dropped significantly. The flow rates < 60 mL/min were not investigated, as preliminary trials showed that the relatively heavy catalyst particles did not circulate efficiently and tended to sediment rather than remain suspended. To explain these data, particle tracing simulations revealed that as flow rate increases (60, 120, and 240 ml/min), residence time shortens dramatically: from 1.78 s to 0.48 s in backward flow, with particle retention in the illuminated region after 5 s dropping from 21% to 6% (Fig. 4D, Fig. S12). This becomes especially critical in plasmonic catalysis, where the initial hot carrier generation and charge redistribution (fs/ps time-scale) are followed by a multistep surface reaction sequence involving substrate adsorption and oxidative addition at Pd sites[16]. While our rough estimate based on turnover frequency (Suppl. Note 3) suggests a full catalytic cycle might occur every ~38 s, recent kinetic studies indicate that even the oxidative addition step alone may require >0.5 s under non-assisted conditions[50]. This highlights a kinetic limitation in which excessively

Open Access Article. Published on 12 December 2025. Downloaded on 1/21/2026 11:08:48 PM.
This article is licensed under a Creative Commons Attribution 3.0 Unported Licence.

Nanoscale Accepted Manuscript

View Article Online
DOI: 10.1039/D5NR03832D

high flow rates reduce the residence time of reactants at the catalyst surface, preventing completion of the full catalytic cycle despite efficient excitation. Backward flow offers the best compromise, enhancing substrate delivery without prematurely displacing reactants from the catalytic interface. Optimal performance was achieved at 60 mL/min; beyond this, residence time falls below the minimum needed for complete plasmonic activation and reaction.

As a result of theoretical and experimental optimization of plasmon-driven Suzuki, we continued our experiments in optimized conditions, namely configuration 3, 60 mL/min flow. The comparison of biphenyl formation in batch and flow reactors under identical illumination and composition conditions demonstrates that continuous flow operation enables higher reaction rates and 3 times faster full conversion (Fig. 3B). These findings align with recent reports on reconfigurable photoflow platforms[46] and Corcoran[51] et al.'s photon-equivalent-based scaling strategy[46] - in showing how tailored reactor geometry and light management can drastically enhance photoreactivity.

To exclude any side photochemical or leached-Pd homogeneous catalysis, the catalyst was removed from the reaction system after 50 min of illumination (50% BP yield). This led to an immediate cessation of biphenyl formation. The product yield remained at the same level during next 3 hours 10 min of reaction (Fig. S13), that confirms that the catalyst must be physically present in the illuminated zone to sustain the reaction, ruling out significant Pd leaching or thermal photoeffects. While our Au@Pd catalyst is designed for heterogeneous plasmonic Suzuki coupling, a mixed pathway involving transient Pd leaching cannot be fully excluded. Such soluble Pd species, if formed, are typically short-lived and may undergo re-adsorption near the catalyst surface[52]. Another control experiment was performed to verify that the observed coupling product originates from cross-coupling (not homocoupling). A control reaction using 4-bromotoluene instead of bromobenzene during 4 hours showed similar results, the main product detected by GC–MS was 4-methylbiphenyl, not biphenyl. This confirms that the reaction proceeds via selective Suzuki-type C–C cross-coupling between the aryl halide and phenylboronic acid and is not a result of undesired homocoupling pathways.

4. Benchmarking of catalytic parameter: AQY and TON

To evaluate the efficacy of plasmon-driven Suzuki coupling, the apparent quantum yield (AQY)[53] and turnover number (TON) were calculated as descriptors of catalyst activity (Table 1). AQYs and TONs were calculated using equations (1-3) and (4), respectively[2]. In batch mode, the catalyst achieved an AQY of 2.3% for biphenyl formation, exceeding previously reported values for bimetallic catalysts irradiated with >420 nm LEDs by a factor of 1.5 to 23[17-21,53]. Reported AQYs in those systems typically range from 0.1% to 9.2%, even when using higher Pd loadings or more intense light sources. Although, the AQY 9.2% at ref[20] is higher than in our case, the TON is much lower. At the same time, the obtained TON = 833 compete only with 1527 values gained by Au-Pd@h-CeO_2 catalyst under Xe lamp illumination (with filter> 420 nm)[19] while AQY in such case left relatively lower. Shifting from batch to flow regime, TON for plasmon-driven Suzuki coupling stayed the same, indicating that the same number of Pd active sites was involved in both cases, but photon utilization was more efficient in flow. AQY increased threefold (6.4 %) in the flow mode compared to batch, this suggests that the improved AQY arises from enhanced light utilization and reactant delivery efficiency, not from an increase in catalytic capacity (Fig. 3B). Thus, the Au@PdNPs-Al_2O_3 demonstrate great catalytic activity in plasmon assisted reaction in flow mode giving better energy utilization with less amount of catalyst.

Table 1. Comparison of AQY and TON of previously reported plasmonic catalytic systems

Open Access Article. Published on 12 December 2025. Downloaded on 1/21/2026 11:08:48 PM.
This article is licensed under a Creative Commons Attribution 3.0 Unported Licence.

Nanoscale Accepted Manuscript

View Article Online
DOI: 10.1039/D5NR03832D

Structure and Pd, wt%	Time, h	Light source wavelength, nm	Laser power, mW cm^{-2}	Yield, % (amount, mmol)	*Apparent quantum yield, %	TON	Ref
Pd93Au7/BiOB, 0.00035	6	400-800	300[a]	99% (0.19)	1.45	465	17
PdAu nanosheets, 0.76	12	Xe lamp	300	99 % (0.25)	0.49	3.44	54
T-Pd@CN/PLA fiber, 0.64	0.67	LED lamp	360	99% (0.495)	0.1	830	18
Au-Pd@h-CeO2, 0.26	3	Xe lamp (filter > 420 nm)	400	94% (0.188)	0.8	1 527	19
Pd/Au NRs-x@rGO[b], 0.80	0.5	LED > 420 nm	100	65% (0.065)	9.2	16	20
AuPd/SiO2,12.5	8	LED > 420 nm	100	79%, (0.063)	0.4	240	21
0.09	**11**	**690**	**300**	**Yield 99% (1.6)**	**2.3**	**833**	**This work batch**
0.09	**4**	**690**	**300**	**Yield 99% (1.6)**	**6.4**	**833**	**This work flow**

*AQY was calculated per 1 cm^2

[a] In the absence of reported data, a laser power of 300 mW cm^{-2} was assumed

[b] Iodobenzene was used instead of bromobenzene in the reaction.

5. Plausible mechanistic contribution of mass transfer into flow-mode plasmon catalysis

First, to confirm the plasmonic origin of catalytic activity in our flow reactor, we evaluated AQY at multiple excitation wavelengths. In addition to used 690 nm LED, 590 nm and 808 nm light sources were used (Fig. S14), which fall outside the main plasmon resonance band of Au@PdNPs-Al_2O_3, produced lower AQY values (5.1% and 2.9%, respectively) compared to 690 nm. In contrast, the highest AQY of 6.4% was achieved at 690 nm, which coincides with the plasmonic absorption peak of the catalyst. Although photons at 590 nm possess higher energy, AQY at 690 nm is higher because of excitation of plasmonic mode hybridized with Pd–Au interfacial states represented by a broad shoulder feature in the UV–Vis spectrum at ≈ 700 nm (Fig. 1F). This observation supports the hypothesis that plasmon excitation are maximized when the illumination matches the hybridized plasmonic resonance. The utilization of 690 nm LED source provided energy transfer via hot electron generation in hybridized Au–

Open Access Article. Published on 12 December 2025. Downloaded on 1/21/2026 11:08:48 PM.
This article is licensed under a Creative Commons Attribution 3.0 Unported Licence.

Nanoscale Accepted Manuscript

View Article Online
DOI: 10.1039/D5NR03832D

Pd modes that due to different electronic behaviors favored formation of an Ohmic contact between the two materials, which is beneficial for carriers transfer[55,56].

Secondly, previous reports on plasmon-driven Suzuki reaction revealed the oxidative addition as rate determining step[57,58]. In bimetallic Au@Pd systems, the Au acts as the plasmonic antenna, generating hot electrons upon light excitation. These hot electrons can transfer across the Au–Pd interface into the Pd shell, increasing its electron density and reactivity[52,53]. Generated carriers are transfered to the aryl halide, promoting C–Hal bond cleavage[1,16] (Fig. 5A). This activation results in the formation of a phenyl radical, which subsequently reacts with Pd(0) to form the aryl–palladium intermediate. Thus, in the Au@Pd system, plasmonic excitation facilitates both electron activation of the Pd surface and substrate activation, driving the oxidative addition step[59,60]. This mechanism is supported by Qi Hao et al., who demonstrated that plasmonic hot electrons mediate the cleavage of the C–Hal bond, a key prerequisite for the coupling reaction[61,62].

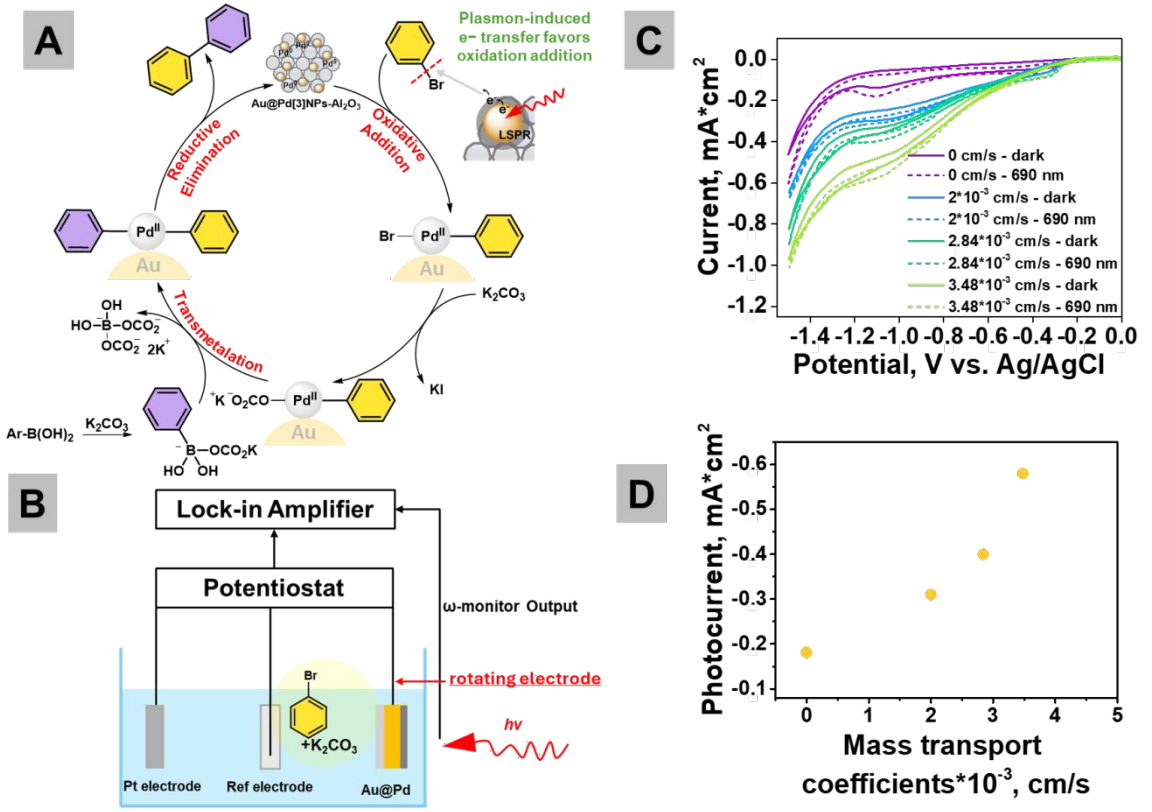

Figure 5. A – Plausible catalytic cycle for plasmon-assisted Suzuki coupling, where under illumination, hot electrons generated by the Au core facilitate oxidative addition of aryl halides at Pd sites, accelerating C–Hal bond cleavage. B - Photoelectrochemical setup to probe light-induced charge dynamics. A three-electrode configuration with Pt counter electrode, Ag/Ag^+ reference electrode, and Au@Pd working electrode is irradiated with 690 nm light to monitor photocurrent response. C – CVA curved measured in dark and under 690 nm LED at different mass transfer coefficients (due to electrode rotation), D – effect of mass transfer coefficient variation to photocurrent produced at 690 nm LED irradiation around −1.1 V vs. Ag/AgCl

To probe the role of mass transport limitations in plasmon-driven Suzuki coupling, we employed photocurrent measurements as an indirect indicator of hot electron transfer efficiency under varying transport conditions (Fig. 5). The aim was to probe whether the rate of reactant delivery to the catalyst surface is crucial for plasmonic chemistry. If the activation of aryl halides by hot electrons is not solely dictated by carrier generation rates, but also by the

Open Access Article. Published on 12 December 2025. Downloaded on 1/21/2026 11:08:48 PM.
This article is licensed under a Creative Commons Attribution 3.0 Unported Licence.

Nanoscale Accepted Manuscript

View Article Online
DOI: 10.1039/D5NR03832D

local concentration of reactive species, then photocurrent responses should exhibit sensitivity to mass transport. By correlating photocurrent with controlled variations in convective flow, we assess to what extent hot electron-driven reactivity is limited by substrate availability at the catalyst interface. To evaluate the hot electron transfer efficiency of the Au@Pd catalyst system under plasmonic excitation, bromobenzene was selected as the molecular probe. We study efficiency of cleaving the C-Br bond under plasmonic condition using the experimental setup (Fig. 5B) based on previous report for hot electron driven chemistry[62].

To evaluate the influence of mass transport on plasmon-assisted C-Br cleave, cyclic voltammetry (CVA) was conducted under LED illumination with variation of rotating disk speed: 100, 200, and 300 rpm, corresponding to calculated mass transfer coefficients[63] (k_m) of 2.01×10^{-3}, 2.84×10^{-3}, and 3.48×10^{-3} cm/s, respectively (Fig. 5C). These values were derived using the Levich equation, assuming diffusion-limited transport in aqueous medium (Suppl. Note 4). In the absence of rotation and illumination, a small cathodic peak is observed around −1.1 V vs. Ag/AgCl (Fig. 5C, Fig. S15), corresponding to the onset of bromobenzene reduction. Upon 690 nm illumination, the photocurrent increases notably, suggesting enhanced activation of the C–Br bond at the Au@Pd surface. This enhancement may originate from plasmon-induced hot electrons injected into bromobenzene or from field-mediated excitation of the molecule or Pd^0 species formed via Au→Pd electron transfer. In contrast, without illumination, the activation is significantly slower, and the current remains lower.

When electrode rotation is introduced to modulate mass transport, an overall increase in current (Fig. 5C, D) is observed across the potential range of −0.25 to −1.5 V, attributed to improved bromobenzene delivery to the electrode surface and thinning of the diffusion layer. Notably, the peak area in the −1.1 V region increases with rotation speed (Fig. 5C, Fig. S15), indicating that plasmon-driven activation could be mass-transport-limited, since enhanced substrate availability leads to a higher extent of plasmon-activated C–Br bond cleavage. These multiple differences in transport capacity explains the enhanced delivery of bromobenzene and supports the hypothesis that short-lived hot-electron-driven reaction intermediates benefit from rapid replenishment of substrate (even k_m of RRDE is a few orders of magnitude lower than for real flow reactor).

Finally, we compared the diffusion-limited flux (J_{diff}) with the experimentally observed plasmon-catalytic flux (J_{PC}) (Fig. S16-17, Table S3 and Suppl. Note 5). The J_{diff} was calculated using Fick's first law based on experimentally derived values for the diffusion coefficient (calculated based on Randles–Sevchik equation[64]), concentration, and diffusion layer thickness (2.95×10^{-9} mol/cm^2/s). The plasmon-catalytic flux J_{PC} was determined from kinetic measurements of product formation normalized to the estimated surface area of illuminated Au@Pd nanoparticles (1.21×10^{-9} mol/cm^2/s). This analysis shows that the observed catalytic flux is the same order as the diffusion-limited value, suggesting mass transport can indeed significantly influence the overall reaction performance. J_{diff} and J_{PC} depend strongly on assumptions such as the diffusion layer thickness and the illuminated catalytic area[65,66]. Because both diffusion and illuminated area vary during operation, the obtained flux values have to be treated with the level of one magnitude of uncertainty.

In plasmonic catalysis, photons act as reactants, and the catalytic rate is ultimately governed by the interplay between molecular diffusion (J_{diff}) and photon delivery rate. Hot electrons are generated (in Au@Pd) within femtoseconds of photon absorption but can only drive catalysis if a reactant is present at the surface within their lifetime. Thus, the observed macroscopic J_{PC} reflects the overlap between fs-scale carrier generation events and reactant arrival via diffusion, integrated over the catalyst surface and reaction time. Although the role of mass transport is recognized in catalysis in general, its significance has been not extensively addressed in plasmonic systems, which have traditionally focused on excited carriers dynamics. To probe this interplay, we scaled the plasmon-driven Suzuki reaction from 20 mL

Open Access Article. Published on 12 December 2025. Downloaded on 1/21/2026 11:08:48 PM.
This article is licensed under a Creative Commons Attribution 3.0 Unported Licence.

Nanoscale Accepted Manuscript

View Article Online
DOI: 10.1039/D5NR03832D

to 40 mL, increasing catalyst and reactants proportionally to maintain constant concentrations. Despite a constant J_{diff}, biphenyl yield declined over 4 hours (99% → 89% → 50%), pointing to a photon flux limitation. As the illuminated area and photon density did not scale accordingly, the frequency of hot carrier generation per site decreased, reducing the probability of overlap with reactants and lowering J_{PC}. This underscores that even with efficient ultrafast excitation, macroscopic reactivity remains limited by the joint supply of molecular and photonic reactants, emphasizing the importance of optimized reactants and light delivery in scalable plasmonic systems. To maintain high yields at larger volumes, future reactor designs should incorporate expanded illuminated surface areas (e.g., modular flat-plate channels), light redistribution elements to minimize shading, and intensified mixing strategies to ensure uniform photon access across the slurry. Such approaches will be essential for translating plasmonic catalysis to scalable, high-throughput operation.

Conclusion.

This study moves plasmonic catalysis beyond its conventional boundaries by bridging plasmon catalysts designing and mechanistic studies with scalable flow concept. Through the integration of gram-scale Au@Pd-Al_2O_3 catalysts into a continuous-flow platform, we demonstrate a high-yield/AQY/TON Suzuki coupling under visible light and establish a mechanistic basis for performance enhancement due to mass transport and photon dynamic/utilization. Crucially, we show that hot electron transfer to molecular reagents, not just across metal-metal interfaces, is essential for rate acceleration in plasmonic chemistry exemplified by Suzuki coupling reaction. By combining CFD-guided flow reactor optimization with photoelectrochemical validation, we uncover that catalytic performance is governed by a balance between photon residence time and substrate accessibility guided by mass transport. The identification of a critical exposure threshold (~0.5–1.0 s) by CFD redefines how future photoreactors must be designed - not merely to illuminate, but to kinetically support plasmon-induced reactivity. For the first time, we showed that plasmon-catalytic flux and diffusion flux are within one order of magnitude, indicating that mass transport is a key limitation and that photon flux alone is insufficient to drive high catalytic turnover if reactants are not continuously delivered.

Beyond demonstrating record catalytic metrics of AQY and TON, this work offers a conceptual shift: light-driven reactions should be engineered as spatiotemporally resolved processes, where dynamic flow not only enhances mass transport but fundamentally could modulate the mechanism of photoactivation. To overcome the observed yield decrease with reaction volume increase, one must scale photon delivery organization. This could include optimizing plasmonic catalyst, light intensity, spatial coverage, residence time, and catalyst accessibility, ensuring that hot carriers generated on the fs scale are effectively coupled with reactants arriving on the ms–s scale.

Author contributions

M.E. and D.V.– Investigation, Data Curation, Visualization, Writing - Original Draft, Validation; E.M. - Investigation, Data Curation, Visualization ; O.G. - Methodology; M. Y. S. I. and D.M. – Resources, Writing - Review & Editing; T. F. and C. K. - Formal analysis, Visualization , Investigation; J. H. M. and M.M.M. - - Formal analysis, Investigation, Writing - Original Draft; M. V. – Resources; O. L. – Supervision; Resources; Writing - Review & Editing; O.G. – Conceptualization; Supervision; Writing - Original Draft.

Data availability

The data supporting this article have been included as part of the Supplementary Information.

Acknowledgment

Open Access Article. Published on 12 December 2025. Downloaded on 1/21/2026 11:08:48 PM.
This article is licensed under a Creative Commons Attribution 3.0 Unported Licence.

Nanoscale Accepted Manuscript

This research was supported by the Russian Science Foundation (project no. 24-73-00127).
This research was funded in part by the Austrian Science Fund (FWF) [10.55776/COE5] (Cluster of Excellence MECS). This work was supported by the Czech Science Foundation (GA CR) under the project no. 23-08509S.

View Article Online
DOI: 10.1039/D5NR03832D

Open Access Article. Published on 12 December 2025. Downloaded on 1/21/2026 11:08:48 PM.
This article is licensed under a Creative Commons Attribution 3.0 Unported Licence.

Nanoscale Accepted Manuscript

View Article Online
DOI: 10.1039/D5NR03832D

Methods.

Materials

Deionized water, methanol (puriss, p.a., absolute, ≥99.8 % (GC)), ethanol (≥99.5% (GC)), chloroauric acid tetrahydrate ($HAuCl_4 \cdot 4H_2O$, 99.9 %), ascorbic acid (AA, 99.0 %), tri-Sodium citrate dihydrate (Na_3C, 99%), aluminum oxide (Al_2O_3, activated, Brockmann I, standard grade, neutral, 199974, 99.5%), palladium(II) chloride ($PdCl_2$, 99%), hydrochloric acid (HCl, 36%), bromobenzene (for synthesis), phenylboronic acid (purum, ≥97.0% (HPLC)), potassium carbonate (K_2CO_3, ACS reagent, ≥99.0%) were purchased from Sigma-Aldrich and used without further purification.

Synthesis of gold nanoparticles (AuNPs).

Gold nanoparticles (AuNPs) were synthesized by microwave assisted method with some modification[30]. Briefly, 1 mL $HAuCl_4$ water solution (0.0254 mmol) and 1 ml of sodium citrate solution (0.0287 mmol) were added to 18 mL H_2O. The resulting solution was placed in a microwave oven for 3 min at 240 W and washes with water.

Synthesis of AuNPs -Al_2O_3

Firstly, the powdered Al_2O_3 was activated with methanol at room temperature (RT) for 30 min and dried at 60 °C. After, 18 mL of distilled water was mixed with 1 mL of $HAuCl_4$ solution (0.0254 mmol), 1 mL of sodium citrate solution (0.0287 mmol) and 1 g of activated powdered Al_2O_3. The resulting solution was placed in a microwave oven for 3 min at 240 W. The AuNPs-Al_2O_3 powder was separated from the solution using a centrifuge (7830 rpm, 10 minutes), washed several times with methanol, and finally dried under vacuum.

Synthesis of Au@Pd[1-4]NPs- Al_2O_3

Pd shell was grown on AuNPs -Al2O3 according to[40]. Briefly, 0.2g AuNPs -Al_2O_3, 1.0 mM H_2PdCl_4 (0.22, 0.55, 1.34 and 2 mL) and water (9.66, 9.15, 7.96 and 7 mL), respectively, were mixed and cooled down in an ice bath. After, 10 mM ascorbic acid (0.12, 0.3, 0.7 and 1 mL) was added slowly and the solutions were left for 15 min. The Au@Pd[1-4]NPs-Al_2O_3 powder was separated from the solution using a centrifuge (7830 rpm, 10 minutes), washed several times with methanol, and finally dried under vacuum.

Upscaling procedures for synthesis Au@Pd[3]NPs- Al_2O_3

3g AuNPs-Al_2O_3, 20 mL of 1.0 mM H_2PdCl_4, 114.4 mL of water were mixed and cooled down in an ice bath. After 10.5 mL of 10 mM ascorbic acid was added slowly and the solution was left for 15 min. The Au@Pd[3]-Al_2O_3 powder was separated from the solution using a centrifuge (7830 rpm, 10 minutes), washed several times with methanol, and finally dried under vacuum.

General procedure for Suzuki reaction in a flask

Suzuki–Miyaura coupling was conducted in a flask (50 ml volume). In a typical reaction, bromobenzene (1.6 mmol, 1 equiv), phenylboronic acid (3.2 mmol, 2 equiv), K_2CO_3 (4.8 mmol, 3 equiv), Au@Pd[3]NPs-Al_2O_3 0.5g were added to 1:1 (v/v) H_2O/EtOH (20 mL). The reaction was stirred continuously under LED 690 nm using a cooling fan to keep temperature approximately 29 °C.

General procedure for Suzuki reaction in a continuous flow mode

Open Access Article. Published on 12 December 2025. Downloaded on 1/21/2026 11:08:48 PM.
This article is licensed under a Creative Commons Attribution 3.0 Unported Licence.

Nanoscale Accepted Manuscript

View Article Online
DOI: 10.1039/D5NR03832D

The Suzuki–Miyaura cross-coupling reaction for the synthesis of biphenyl was carried out in a custom-designed photochemical flow reactor provided by Redeem Solar Technologies GmbH. This laboratory-scale reactor is constructed from stainless steel and features a rectangular flow channel equipped with arrow-shaped static mixing elements (see Fig. 3A). The flow channel is sealed with an 8 mm-thick borosilicate glass window, providing a total window area of 26.4 cm² and an illuminated channel area of 20.8 cm². The depth of the illuminated flow channel is 1 mm, resulting in a total illuminated reactor volume of 2.08 cm³. Sealing is achieved using a Viton O-ring, and the reactor is mounted on a commercially available stand from the manufacturer, tilted at an angle of 60° along the inlet–outlet axis. A peristaltic pump is used to circulate the slurry from the reactor to a stirred glass vial and back. The slurry is introduced into the reactor through the bottom inlet and flows upward toward the top outlet. The reactor is irradiated using the same light source as employed for batch reactor screening experiments and is cooled using a fan to maintain the reactor temperature within the range of 25–28 °C. The Arrow Reactor was investigated under two distinct configurations: (1) arrows aligned in the direction of flow (upward orientation) and (2) arrows oriented counter to the flow direction (downward orientation). These two configurations were also repeated with the slurry introduced from the top of the reactor, yielding four experimental conditions in total.

In a typical experiment, bromobenzene (1.6 mmol, 1 equiv), phenylboronic acid (3.2 mmol, 2 equiv), and potassium carbonate (K_2CO_3, 4.8 mmol, 3 equiv) were dispersed in a 1:1 (v/v) H_2O/EtOH solvent mixture (20 mL total volume). The heterogeneous catalyst, Au@Pd[3]NPs supported on Al_2O_3 (0.5 g), was added to the reaction mixture, which was subsequently pumped through the reactor using a peristaltic pump (flow rate of 60 mL/min).

The reactor was continuously irradiated with a 690 nm LED light source (300 mW/cm²) at 1 cm distance from the reaction mixture for 4 hours while being actively cooled using an axial fan (D1K1 AC 220 V PC Fan) to maintain thermal stability.

Quantitative analysis of biphenyl was performed by gas chromatography–mass spectrometry (GC–MS). The sampling (0.5 mL) was performed in certain period of time, and aliquot was extracted with hexane (1 mL). A sample of the reaction mixture was taken and analyzed via GC–MS on a Shimadzu Nexis 2030 gas chromatograph equipped with an SH-5MS capillary column (30 m × 0.25 mm i.d., 0.25 μm film thickness). Helium was used as the carrier gas at a pressure of 119.0 kPa and a linear velocity of 49.7 cm/s. 40 °C (2 min) → 20 °C/min (280 °C) → 280 °C (8 min). The injection volume was 1 μL, with a split ratio of 40:1.. The inlet temperature was 280 °C , and the *m*/*z* range was 10 to 500. GC calibration was performed before each series of experiments to ensure quantitative accuracy.

Control experiment in the dark

Bromobenzene (1.6 mmol, 1 equiv), phenylboronic acid (3.2 mmol, 2 equiv), and potassium carbonate (K_2CO_3, 4.8 mmol, 3 equiv) were dispersed in a 1:1 (v/v) H_2O/EtOH solvent mixture (20 mL total volume). The heterogeneous catalyst, Au@Pd[3]NPs-Al_2O_3 (0.5 g), was added to the reaction mixture, which was subsequently pumped through the reactor using a peristaltic pump (flow rate of 60 mL/min) for 4 hours.

Control experiment without catalyst

Bromobenzene (1.6 mmol, 1 equiv), phenylboronic acid (3.2 mmol, 2 equiv), and potassium carbonate (K_2CO_3, 4.8 mmol, 3 equiv) were dispersed in a 1:1 (v/v) H_2O/EtOH solvent mixture (20 mL total volume), which was subsequently pumped through the reactor using a peristaltic pump (flow rate of 60 mL/min) for 4 hours.

Open Access Article. Published on 12 December 2025. Downloaded on 1/21/2026 11:08:48 PM.
This article is licensed under a Creative Commons Attribution 3.0 Unported Licence.

Nanoscale Accepted Manuscript

View Article Online
DOI: 10.1039/D5NR03832D

Control Experiment with bromotoluene

Suzuki–Miyaura coupling was conducted in a flask (50 ml volume). In a typical reaction, bromotoluene (1.6 mmol, 1 equiv), phenylboronic acid (3.2 mmol, 2 equiv), K_2CO_3 (4.8 mmol, 3 equiv), Au@Pd[3]NPs-Al_2O_3 0.5g were added to 1:1 (v/v) H2O/EtOH (20 mL). The reaction was stirred continuously under LED 690 nm using a cooling fan to keep temperature approximately 29 °C.

Photocamera measurement

The surface temperature changes during the experiment were monitored using a FLIR E5 infrared camera.

Procedure to calculate AQY

The apparent quantum yield (AQY) was calculated according to the following equation:

$$AQY = \frac{n_{biphenyl}}{n_{inced\ photons}} \cdot 100\% \quad \text{(eqn. 1)}$$

where n_{biphenyl} are the moles of formed biphenyl and $n_{inced\ photons}$ is the moles of incident photons.

The number of incident photons (in moles) was calculated from measured power and averaged photons energy.

$$n_{inced\ photons} = \frac{E_{total}}{E_{photon} \cdot N_A} = \frac{t \cdot P_{LED} \cdot \lambda}{N_a \cdot c \cdot h} \cdot 100\ \% \quad \text{(eqn. 2)}$$

where λ is the wavelength of the light (m), P is power of the light source (W), t is the reaction time under illumination (s), h is Planck's constant (6.63×10^{-34}J\s), c is the speed of light (2.998×10^8 m/s), N_A is Avogadro's number (6.022×10^{23} mol^{-1}).

In case of the Xe lamp, the averaged photon energy was calculated as a weighted sum of the photon energies at each wavelength (E=hc/λ), using the normalized spectral irradiance (Fig. S18) to represent the relative contribution of each wavelength to the total irradiance [36].

For example, Ephoton corresponding to the irradiance range of 400–800 nm was calculated as

$$\text{Ephoton}_{\text{(400-800 nm)}} = \sum_{i=400}^{800} \left(\frac{E_{\lambda i} \cdot h \cdot c}{\sum_{400}^{800} E\lambda_i \cdot \lambda i} \right) \cdot 100\ \% \quad \text{(eqn. 3)}$$

Where $E\lambda_i$ is Spectral irradiance for each wavelength, $W \cdot m^{-2} \cdot nm^{-1}$

The main aim was to compare the photocatalytic performance with literature data, AQY was determined using a standard irradiated area of 1 cm².

Calculation of the turnover number (TON)

The TON values were calculated as a ratio nproduct/ncat, where nproduct is the mole number of the obtained product (biphenyl) and ncat is the mole number of the catalytic centers (Pd).

$$\text{TON} = n_{product}/n_{Pd} \quad \text{(eqn. 4)}$$

Transmission electron microscopy (TEM) photos were collected using a FEI/ThermoFisher (TFS) Tecnai G2 20 (S)TEM equipped with an X-FEG electron source and operated at 200 kV acceleration voltage. The STEM-EDX measurements were done using an EDAX Appollo XLT windowless 30 mm² SDD detector with an energy resolution of 132.9 eV.

Open Access Article. Published on 12 December 2025. Downloaded on 1/21/2026 11:08:48 PM.
This article is licensed under a Creative Commons Attribution 3.0 Unported Licence.

Nanoscale Accepted Manuscript

View Article Online
DOI: 10.1039/D5NR03832D

UV-Vis absorption spectra were collected using an HR2000 (Ocean Optics) spectrometer in the 400 – 1000 nm wavelength range with AvaLight-DHS light source (Avantes).

X-ray diffraction data were collected on an XRD-diffractometer PAN analytical X ´PertPRO using Cu K αradiation (1.5406 ˚A).

X-ray photon spectroscopy (XPS) spectra were recorded on a Thermo Fisher Scientific XPS NEXSA spectrometer equipped with an Al K Alpha X-ray monochromatic emitter with an energy of 1486.6 eV. Survey spectra were recorded using pass energy of 200 eV with energy resolution of 1 eV. The spectra were calibrated against the C1s peak set at 284.8 eV. High-resolution spectra (O1s, Al2p, Pd3d, Au4f) were collected using pass energy of 50 eV and a resolution of 0.1 eV. The concentrations of elements were calculated in at. % using the sensitivity factors provided by the manufacturer.

Scanning electron micrographs were recorded using a Sigma HD-VP (Zeiss, Germany) with a Everhart Thornley SE-electron Detector. Powders was fixed with carbon tape to the sample holder and analyzed without further pretreatment. Micrographs were obtained at 2–15 kV and 3.5–8.9 mm working distance.

Atomic adsorption spectroscopy (AAS) was collected on AGILENT 280 FS AA SPECTROMETER (Agilent Technologies Australia).

CFD simulations.

Finite Element (FEM) simulations were performed using the CFD Module of Comsol running on a workstation PC. Laminar flow was assumed as the corresponding Reynolds Number of the structures where with ~20 small enough to only consider turbulent flow using a k-ε approximation. Particle Tracing was performed afterwards using the obtained Flow Profiles for forward and backward flow, therefore ignoring back action of the particles on the fluid. The Residence times were computed by taking the average of the integral of the time steps from the entry point to the exit at the outlet. The particles stayed in the reactor resulting in a statistical spread of around 6%. For computational reasons particles that had collision with a wall where not further acknowledged in the process and not considered for the average. This is assumed to be a valid approximation as the residence times with and without wall collision could be shown to be very similar.

Electrochemical measurements

All electrochemical experiments were performed in a standard three-electrode cell. Ag/AgCl (3M KCl) was used as the reference electrode, a platinum spring served as the counter electrode, and the working electrode was made of glassy carbon. Au@Pd-Al_2O_3 particles were applied to the working electrode as follows: a suspension of particles in methanol (300 µl) was mixed with 5 µl of a 5% solution of Nafion, after which the resulting solution was subjected to ultrasonic treatment for 5 minutes. Then, 10 µl of the prepared suspension was applied dropwise to the glassy carbon electrode and dried at 50 °C for 20 minutes. The electrolyte was a water-ethanol solution containing 0.1 M K_2CO_3 and bromobenzene at a concentration of 0.18 M. During the experiment, the sample was illuminated with a LED (690 nm, 300 mW/cm^2). All electrochemical studies were performed using a RRDE rotary system (100, 200, and 300 rpm) manufactured by IVIUM Technologies.

Computational methodology

All optical simulations were performed using the TERMS (T-matrix for Electromagnetic Radiation with Multiple Scatterers) framework using the superposition *T*-matrix specifically designed for nanoplasmonic systems. The TERMS platform solves Maxwell's equations in the

Open Access Article. Published on 12 December 2025. Downloaded on 1/21/2026 11:08:48 PM.
This article is licensed under a Creative Commons Attribution 3.0 Unported Licence.

Nanoscale Accepted Manuscript

View Article Online
DOI: 10.1039/D5NR03832D

frequency domain using a surface integral formulation, which enables accurate modelling of complex core-shell geometries and near-field interactions between closely spaced nanostructures. Core-shell dimer systems were modelled as spherical Au@Pd nanoparticles consisting of a gold core (20 nm radius) surrounded by a 3 nm palladium shell. The interparticle edge-to-edge spacing was varied between 3 nm and 5 nm by adjusting the center-to-center distance of the two spheres. The dielectric environment was modelled as homogeneous with a refractive index of 1.7689, corresponding to a typical aqueous or alcohol-based solvent. Far-field scattering and absorption cross-sections were computed by enabling the *cross_sections* output option in TERMS, using *ModeAndScheme 2 2* and a multipole cutoff of 20. For near-field analysis, the electric field intensity ($|E|^2$) and its derived quantities were mapped over a 2D plane (z = 0) using the MapQuantity 2 E directive and a spatial resolution of 600×600 points in a 140 nm × 140 nm region. Material dispersion was included via dielectric function files, based on experimentally measured optical constants. The Raman enhancement factor was computed as $|E|^4$ from the simulated local electric field intensities, consistent with the electromagnetic enhancement mechanism in surface-enhanced Raman scattering (SERS). Hot carrier generation was estimated using a simplified proxy, $\mathrm{Im}(\varepsilon) \times |E|^2$, where the imaginary part of the complex dielectric function represents material losses contributing to non-radiative plasmon decay. The spatial distribution of this quantity was used to evaluate the localization and efficiency of hot carrier excitation within the Pd shell. All visualizations and post-processing analyses, including extraction of enhancement maps and hot carrier distributions, were carried out in **R** using custom scripts built around the *rhdf5, ggplot2*, and *viridis* packages.

References.

1. A. Gellé, T. Jin, L. de la Garza, G. D. Price, L. V. Besteiro and A. Moores, *Chem. Rev.*, 2019, **120**, 986-1041.
2. D. Votkina, A. Trelin, V. Semin, O. Lyutakov, V. Svorcik, P. Petunin, G. Audran, S. R. Marque, O. Guselnikova and P. Postnikov, Technology, *Catal. Sci. Technol.*, 2024, **14**, 3707-3718.
3. C. Han, B. K. Kundu, Y. Liang and Y. Sun, Adv. Mater., 2024, 36, 2307759.
4. N. S. Lewis, G. Crabtree, A. J. Nozik, M. R. Wasielewski, P. Alivisatos, H. Kung and R. Ellingson, *Basic Research Needs for Solar Energy Utilization, Report of the Basic Energy Sciences Workshop on Solar Energy Utilization*, DOESC (USDOE Office of Science (SC)), 2005.
5. O. Guselnikova, G. Audran, J.- P. Joly, A. Trelin, E. V. Tretyakov, V. Svorcik, O. Lyutakov, S. R. Marque and P. Postnikov, *Chem. Sci.*, 2021, **12**, 4154-4161.
6. D. Votkina, P. Petunin, E. Miliutina, A. Trelin, O. Lyutakov, V. Svorcik, G. Audran, J. Havot, R. Valiev, L.I. Valiulina, J. - P. Joly, Y. Yamauchi, J. H. Mokkath, J. Henzie, O. Guselnikova, S. R. A. Marque and P. Postnikov, *ACS Catal.*, 2023, **13**, 2822-2833.
7. S. Cañellas, M. Nuño and E. Speckmeier, Improving reproducibility of photocatalytic reactions—how to facilitate broad application of new methods, *Nat. Commun.*, 2024, 15, 307.
8. E. Cortés, L. V. Besteiro, A. Alabastri, A. Baldi, G. Tagliabue, A. Demetriadou and P. Narang, *ACS Nano*, 2020, **14**, 16202-16219.
9. A. G. da Silva, T. S. Rodrigues, J. Wang and P.H. Camargo, *Chem. Commun.*, 2022, **58**, 2055-2074.
10. W. Jiang, B. Q. L. Low, R. Long, J. Low, H. Loh, K. Y. Tang, C. H. T. Chai, H. Zhu, H. Zhu, Z. Li, X. J. Loh, Y. Xiong and E. Ye, *ACS Nano*, 2023, **17**, 4193-4229.
11. R. A. Adomaitis, *Comput. Aided Chem. Eng*., 2025, 192, 108873.
12. O. Guselnikova, J. Váňa, L. T. Phuong, I. Panov, L. Rulíšek, A. Trelin, P. Postnikov, V. Švorčík, E. Andris and O. Lyutakov, *Chem. Sci*., 2021, **12**, 5591-5598.

Open Access Article. Published on 12 December 2025. Downloaded on 1/21/2026 11:08:48 PM.
This article is licensed under a Creative Commons Attribution 3.0 Unported Licence.

Nanoscale Accepted Manuscript

View Article Online
DOI: 10.1039/D5NR03832D

13. Y. Fu, N. A. Simeth, W. Szymanski and B.L. Feringa, *Nat. Rev. Chem*., 2024, **8**, 665-685.
14. A. Srivastava, H. Kaur, H. Pahuja, T. Rangarajan, R. S. Varma and S. Pasricha, *Coord. Chem. Rev*., 2024, **507**, 215763.
15. C. Torborg and M. Beller, *Adv. Synth. Catal.*, 2009, **351**, 3027-3043.
16. F. Wang, C. Li, H. Chen, R. Jiang, L. -D. Sun, Q. Li, J. Wang, J. C. Yu and C. - H. Yan, *J. Am. Chem. Soc*., 2013, **135**, 5588-5601.
17. É. Casey, J. D. Holmes and G. Collins, *ACS Appl. Nano Mater*., 2022, **5**, 16196-16206.
18. T. Xu, C. Li, M. Qian, W. Chen and W. Lu, *Mol. Catal*., 2023, **545**, 113207.
19. X. Zhao, S. Wang, K. Yang, X. Yang, X. Liu and I. Science, *J. Colloid Interface Sci*., 2023, **633** 11-23.
20. P. Verma, K. Tamaki, T. Shimojitosho, T. Yoshii, Y. Kuwahara, K. Mori and H. Yamashita, *Catal. Today,* 2023, 410, 332-339.
21. M. - Y. Qi, H. - K. Wu, M. Anpo, Z. - R. Tang and Y. - J. Xu, *Nano Res.*, 2022, **15**, 9967-9975.
22. Q. Xiao, S. Sarina, A. Bo, J. Jia, H. Liu, D. P. Arnold, Y. Huang, H. Wu and H. Zhu, *ACS Catal*., 2014, **4**, 1725-1734.
23. I. - W. Un and Y. Sivan, *ACS Photonics*, 2021, **8**, 1183-1190.
24. J. W. Pickering, V. R. Bhethanabotla and J. N. Kuhn, *Chem. Eng. J.*, 2017, **314**, 11-18.
25. O. Henrotte, S. Kment and A. Naldoni, *Nano Lett*., 2024, **24**, 8851-8858.
26. C. G. Thomson, A. - L. Lee and F. Vilela, *Beilstein J. Org. Chem.*, 2020, **16**, 1495-1549.
27. S. L. Rachel Cassidy Elias, US Pat., 20240091732A1, 2023.
28. T. Noël, M. Escriba Gelonch and K. Huvaere, Industrial Photochemistry: From laboratory Scale to Industrial Scal, in *Photochemical Processes in Continuous-Flow Reactions*, ed. T. Noël, World Scientific, Singapore, 2017, 245–267.
29. Y. Zhao, C. Ding, J. Zhu, W. Qin, X. Tao, F. Fan, R. Li and C. Li, *Angew. Chem. Int. Ed.*, 2020, **59**, 9653-9658.
30. E. Cortés, R. Grzeschik, S. A. Maier and S. Schlücker, *Nat. Rev. Chem*., 2022, **6**, 259-274.
31. S. Ullah, E. P. Ferreira-Neto, A. A. Khan, I. P. Medeiros and H. Wender, *Photochem. Photobiol. Sci*., 2023, **22**, 219-240.
32. B. R. Gangapuram, R. Bandi, M. Alle, R. Dadigala, G. M. Kotu and V. Guttena, *J. Mol. Struct*., 2018, **1167**, 305-315.
33. C. - Y. Chiu, M. - Y. Yang, F. - C. Lin, J. - S. Huang and M. H. Huang, *Nanoscale*, 2014, **6**, 7656-7665.
34. O. Guselnikova, A. Olshtrem, Y. Kalachyova, I. Panov, P. Postnikov, V. Svorcik and O. Lyutakov, *J. Phys. Chem. C*, 2018, **122**, 26613-26622.
35. G. V. Nachiyar, T. Surendra, V. Kalaiselvi, R. Rajagopal, P. Kuppusamy, N. Basavegowda and S. M. Roopan, *Optik*, 2022, **267**, 169633.
36. X. Ren, Y. Song, A. Liu, J. Zhang, P. Yang, J. Zhang and M. An, *RSC Adv.*, 2015, **5**, 64997-65004.
37. S. K. Ghosh, S. Nath, S. Kundu, K. Esumi and T. Pal, *J. Phys. Chem. B*, 2004, **108**, 13963–13971.
38. S. De Marchi, S. Núñez-Sánchez, G. Bodelón, J. Pérez-Juste and I. Pastoriza-Santos, *Nanoscale*, 2020, **12**, 23424-23443.
39. Lighthouse. Spectrum library. https://www2.pvlighthouse.com.au/resources/optics/spectrum%20library/spectrum%20library.aspx, (accessed September 2025).
40. J. - W. Hu, J. - F. Li, B. Ren, D. - Y. Wu, S. - G. Sun and Z.-Q. Tian, *J. Phys. Chem. C*, 2007, **111**, 1105-1112.
41. W. - H. Liu, J. - W. Luo, S. - S. Li and L. - W. Wang, *npj Comput. Mater*., 2021, **7**, 117.

Open Access Article. Published on 12 December 2025. Downloaded on 1/21/2026 11:08:48 PM.
This article is licensed under a Creative Commons Attribution 3.0 Unported Licence.

Nanoscale Accepted Manuscript

View Article Online
DOI: 10.1039/D5NR03832D

42. P. Christopher, H. Xin, A. Marimuthu and S. Linic, *Nat. Mater.*, 2012, **11**, 1044-1050.
43. G. Baffou and R. Quidant, *Chem. Soc. Rev.*, 2014, **43**, 3898-3907.
44. B. N. Reinecke, K. P. Kuhl, H. Ogasawara, L. Li, J. Voss, F. Abild-Pedersen, A. Nilsson and T. F. Jaramillo, *Surf. Sci.*, 2016, **650**, 24-33.
45. J. Chastain, *Handbook of X-ray Photoelectron Spectroscopy*, PerkinElmer Corp., Minnesota, 1992, 234
46. F. Ehrlich-Sommer, T. Friedl, C. Koller and M. Y. S. Ibrahim, React. Chem. Eng., 2025, 10, 959-964.
47. D. Chen, F. Li and A. K. Ray, *Catal. Today*, 2001, **66**, 475–485
48. Z. Zhang, C. Zhang, H. Zheng and H. Xu, *Acc. Chem. Res.*, 2019, **52**, 2506-2515.
49. C. Tien, in *Introduction to Adsorption*, Elsevier, Amsterdam, 2019, 4, 87-118.
50. K. Vikse, T. Naka, J. S. McIndoe, M. Besora and F. Maseras, *ChemCatChem*, 2013, **5**, 3604-3609.
51. E. B. Corcoran, J. P. McMullen, F. Lévesque, M. K. Wismer and J. R. Naber, *Angew. Chem., Int. Ed.*, 2020, 59, 11964-11968.
52. N. A. Nemygina, L. Z. Nikoshvili, I. Y. Tiamina, A. V. Bykov, I. S. Smirnov, T. LaGrange, Z. Kaszkur, V. G. Matveeva, E. M. Sulman and L. Kiwi-Minsker, *Org. Process Res. Dev.*, 2018, **22**, 1606-1613.
53. H. Kisch and D. Bahnemann, *J. Phys. Chem. Lett.*, 2015, **6**, 1907-1910.
54. J. Guo, S. Pan, D. Liu and B. B. Mamba, J. Gui, *ACS Appl. Nano Mater.*, 2024, **7**, 22081-22092.
55. L. Zhou, Q. Huang and Y. Xia, *Chem. Rev.,* 2024, **124(14)**, 8597–8619
56. B. Jeon, D. Kim, T. S. Kim, H. K. Lee and J.Y. Park, *ACS Appl. Mater. Interfaces,* 2023, **15**, 52392–52400
57. D. B. Eremin and V. P. Ananikov, *Coord. Chem. Rev.*, 2017, **346**, 2-19.
58. N. Miyaura and A. Suzuki, *Chem. Rev.*, 1995, **95**, 2457-2483.
59. M. Wen, S. Takakura, K. Fuku, K. Mori and H. Yamashita, *Catal. Today*, 2015, **242**, 381-385.
60. H. - S. Feng, F. Dong, H. - S. Su, M. M. Sartin and B. Ren, *J. Appl. Phys.*, 2020, **128**, 173105.
61. T. Yoshii, Y. Kuwahara, K. Mori and H. Yamashita, *J. Phys. Chem. C*, 2019, **123**, 24575-24583.
62. Y. Wei, D. Chen, X. Fan, X. Tang, L. Yao, X. Zhao, Q. Li, J. Wang, T. Qiu and Q. Hao, *ACS Catal.*, 2024, **14**, 15043-15051.
63. Y. Wang, L. Shen, Y. Wang, B. Hou, G. N. Gibson, N. Poudel, J. Chen, H. Shi, E. Guignon, N. C. Cady, W. D. Page, A. Pilar, J. Dawlaty and S. B. Cronin, *Faraday Discuss.*, 2019, **214**, 325-339.
64. V. Alopaeus and H. V. Norden, *Comput. Chem. Eng.*, 1999, **23**, 1177-1182.
65. M. Motegh, J. Cen, P. W. Appel, J. R. van Ommen and M. T. Kreutzer, *Chem. Eng. J.*, 2014, **247**, 314–319.
66. N. A. B. Timmerhuis, J. A. Wood and R. G. H. Lammertink, *Chem. Eng. Sci.*, 2021, **245**, 116835.

Open Access Article. Published on 12 December 2025. Downloaded on 1/21/2026 11:08:48 PM.
This article is licensed under a Creative Commons Attribution 3.0 Unported Licence.

Nanoscale Accepted Manuscript

The data supporting this article have been included as part of the Supplementary Information.

View Article Online
DOI: 10.1039/D5NR03832D

Open Access Article. Published on 12 December 2025. Downloaded on 1/21/2026 11:08:48 PM.
This article is licensed under a Creative Commons Attribution 3.0 Unported Licence.

Nanoscale Accepted Manuscript